



## Controllable synthesis of mesoporous manganese oxide microsphere efficient for photo-Fenton-like removal of fluoroquinolone antibiotics



Anqi Wang<sup>a</sup>, Hui Wang<sup>b</sup>, Hao Deng<sup>a</sup>, Shu Wang<sup>c</sup>, Wei Shi<sup>a</sup>, Zixiao Yi<sup>a</sup>, Rongliang Qiu<sup>a</sup>, Kai Yan<sup>a,\*</sup>

<sup>a</sup> Guangdong Provincial Key Laboratory of Environmental Pollution and Remediation Technology, School of Environmental Science and Engineering, Sun Yat-sen University, Guangzhou, 510275, China

<sup>b</sup> College of Chemistry and Environmental Engineering, Shenzhen University, Shenzhen, 518060, China

<sup>c</sup> School of Materials Science and Engineering, Sun Yat-sen University, Guangzhou, 510275, China

### ARTICLE INFO

#### Keywords:

Mesoporous MnO<sub>x</sub> microsphere  
Peroxymonosulfate  
Photo-Fenton-like process  
Fluoroquinolone antibiotics  
Mechanism

### ABSTRACT

Controllable synthesis of mesoporous manganese oxide (MnO<sub>x</sub>) microsphere is successfully achieved using a soft-template P123 assisted method. The as-obtained MnO<sub>x</sub> materials are highly efficient and versatile to remove the category of fluoroquinolone antibiotics (i.e., ofloxacin, ciprofloxacin, enrofloxacin and levofloxacin) using peroxyomonosulfate (PMS) as the oxidant under UV or simulated sunlight irradiation. The mesoporous Mn<sub>3</sub>O<sub>4</sub> microsphere prepared in the presence of 2 g P123 (P<sub>2</sub>-Mn<sub>3</sub>O<sub>4</sub>) exhibits the superior catalytic activity with almost perfect degradation for the fluoroquinolone antibiotics in 10 min under UV irradiation. Moreover, under simulated sunlight irradiation, 74.5% of ofloxacin, 79.4% of ciprofloxacin, 72.3% of enrofloxacin and 81.9% of levofloxacin can be degraded by P<sub>2</sub>-Mn<sub>3</sub>O<sub>4</sub> in 10 min. Besides, the P<sub>2</sub>-Mn<sub>3</sub>O<sub>4</sub> catalyst maintains stable without the obvious deactivation of catalytic activity or structural change after several successive runs, and slight leaching of Mn ions is observed. The ESR spectra further document that SO<sub>4</sub><sup>·-</sup>, OH, O<sub>2</sub><sup>·-</sup> and <sup>1</sup>O<sub>2</sub> radicals are prominent in the decomposition process of antibiotic molecules. In the end, the reaction kinetic and rational degradation pathway are also investigated and proposed.

### 1. Introduction

Pharmaceuticals and personal care products (PPCPs), including various synthetic antibiotics, have brought serious threat to ecological environment and human health because of their increasing occurrence in the aquatic environment [1–4]. As a class of extensively used antibiotics, fluoroquinolones (FQs) are frequently identified in municipal wastewater, surface water and groundwater [5–7]. Recent studies have demonstrated the residuals of FQs in the water bodies often induced the development of fluoroquinolone-resistant bacteria, which caused potential hazardous effects on humans and all the other organisms [8,9]. Unfortunately, FQs are refractory to biodegradation, making traditional sewage treatment plants (STPs) unsuitable for the removal of them, and consequently, FQs residues are continuously released and induced serious environment issue [10–14]. Therefore, it is highly desirable to develop promising technologies with features of low-cost and high-performance for the purification of FQs-contaminated water.

So far, different remediation techniques (e.g., adsorption, biological processes, membrane processes and advanced oxidation processes (AOPs)) aimed at the removal of PPCPs from wastewater have been

developed [15–18]. Among these advanced techniques, hydroxyl radical-AOPs (OH-AOPs), e.g., Fenton process, are considered to be capable of degrading refractory contaminants. However, the application of conventional Fenton process (e.g., Fe<sup>2+</sup>/H<sub>2</sub>O<sub>2</sub>) may suffer from several challenges of the formation of iron-rich sludge, narrow available pH range (2.8–3.5), non-selective oxidation as well as low hydrogen peroxide utilization efficiency, which makes the removal efficiency decrease and increases the treatment costs and complexity [8,19]. Compared with Fenton process, sulfate radical-based AOPs (SO<sub>4</sub><sup>·-</sup>-AOPs) exhibit comparable or even higher standard redox potential (2.5–3.1 V), better selectivity, longer half-life and wider range of pH [20–23]. Thus, SO<sub>4</sub><sup>·-</sup>-AOPs have been frequently utilized to destructively remove highly recalcitrant and non-biodegradable contaminants.

Recent studies have shown that persulfate (PS) and peroxyomonosulfate (PMS) can be activated to generate SO<sub>4</sub><sup>·-</sup> by various methods (e.g., ultraviolet and visible light, electrolysis) over several widely used candidates (e.g., carbon materials, transition metal ions and oxides) [7,24–26]. Among these candidates, activation on transition metal oxides is attractive owing to the high degradation performance, mild reaction conditions and low-cost. Due to its unique

\* Corresponding author.

E-mail address: [yank9@mail.sysu.edu.cn](mailto:yank9@mail.sysu.edu.cn) (K. Yan).

properties of abundant availability, lower toxicity and the multivalent nature,  $\text{MnO}_x$ -based materials have been frequently utilized for the water purification [27,28]. Besides, recent theoretical and experimental studies have demonstrated that the catalytic performances of  $\text{MnO}_x$  have a close relationship with their structure and morphology [29–33]. On the other hand, light-induced activation of PS/PMS has been considered as cost-effective and environment-friendly strategy for the degradation of pollutants. However, little attention has been paid to control the crystal structure of  $\text{MnO}_x$  and tune the photo-Fenton-like system ( $\text{MnO}_x/\text{SO}_4^{2-}/\text{light}$ ) to versatiliely remove the class of FQs antibiotics.

As a structure directing agent, amphiphilic tri-block copolymer P123 (poly(ethylene glycol)-block-poly(propylene glycol)-block-poly(ethylene glycol)) has two medium-length hydrophilic poly(ethylene oxide) groups and a long hydrophobic poly(propylene oxide) segment. Besides, a strong complexing capacity existed between metal ions and P123 will assist the homogeneous dispersion of metal ions and form metal ions-P123 micelles as the backbone to assemble the mesoporous microsphere structure [33–35]. Herein, we documented the controllable synthesis of mesoporous  $\text{MnO}_x$  microsphere by a facile P123-assisted solvothermal approach. The as-obtained  $\text{MnO}_x$  materials were highly efficient to degrade a category of FQs antibiotics. Various synthetic parameters on the physical properties, morphology and texture were investigated by a combination analysis of XRD, BET, XPS, SEM and TEM. The controllable synthesis of mesoporous  $\text{Mn}_3\text{O}_4$  and  $\text{MnO}$  microspheres can be selectively achieved via the calcination in air or Ar. The typical second-generation FQs antibiotics (i.e., ofloxacin (OFL), ciprofloxacin (CIP), enrofloxacin (ENR) and levofloxacin (LEV)) were chosen as the target contaminants and investigated in details. Besides, the degradation reaction kinetics and the degradation pathway were also rationally studied. This work provides a good guideline to design the robust catalyst to remediate the antibiotic-contaminated natural water.

## 2. Experimental section

### 2.1. Material synthesis

The chemical source and purity are described in Supplementary Information (SI). The mesoporous  $\text{MnO}_x$  microsphere was prepared by the facile solvothermal route using P123 as the structure directing agent. Briefly, a certain amount of P123 was dissolved into 40 mL ethanol in a 125 mL Nalgene PVP bottles under vigorous stirring at 40 °C until the solution became clear. After this, 0.5 g manganese acetate tetrahydrate ( $\text{MnAc}_2$ ) was added, followed by stirring and sonication for 30 min, 2.0 g urea with 1 mL  $\text{H}_2\text{O}$  was further added to promote the esterification reaction. The mixture was then transferred into 100 mL Teflon-lined stainless steel autoclave, sealed for solvothermal treatment at 120 °C, and maintained for 6 h. After that, the autoclave was naturally cooled down to room temperature, followed by centrifugation for two times and washed by ethanol several times to remove impurities. The obtained gel was placed and dried in an electric oven at 120 °C for 4 h. Finally, the dried dark brown gel was calcined at 450 °C for 3 h with a heating rate of 5 °C min<sup>-1</sup> under air or Ar atmosphere. Subsequently, the effect of calcining atmosphere and different amount of P123 on the crystalline phase, specific surface area, porous structure, morphology, texture and catalytic activity were thoroughly studied. By changing the amount of P123 (0, 1.0, 2.0 and 4.0 g) and the calcined environment (Ar or air), the finally obtained products were abbreviated as  $\text{P}_0\text{-MnO}_x$ ,  $\text{P}_1\text{-MnO}_x$ ,  $\text{P}_2\text{-MnO}_x$ ,  $\text{P}_4\text{-MnO}_x$ , respectively.

### 2.2. Characterizations

The crystalline phase was firstly studied using powder X-ray diffraction (XRD, Rigaku D-MAX 2200 VPC) equipped with a diffractometer of  $\text{Cu K}\alpha$  radiation operating at a 40 kV, 26 mA, and the

data were collected from 10° to 90° with a step width of 0.02°/θ. The Brunauer-Emmett-Teller (BET) surface area and pore size distribution were analyzed by a Microtrac BELSORP-max adsorption instrument, and samples were out-gassed under a vacuum at 200 °C for 6 h prior to the measurements. The morphology of the prepared mesoporous  $\text{MnO}_x$  microspheres were investigated by scanning electron microscopy (SEM, ZEISS Gemini 500) with an acceleration voltage of 10 kV. The structural information was further studied by transmission electron microscopy (TEM, FEI Tecnai G2 F30) operated at 200 kV. The surface chemical states of mesoporous  $\text{MnO}_x$  microspheres were measured with an X-ray photoelectron spectrometer (XPS, Thermo Electron Corporation ESCALAB250) with  $\text{Al K}\alpha$  source. Electron spin response (ESR) spectra were recorded on a Bruker A300-10/12 spectrometer, and 5,5-di-methyl-1-pyrrolidine -N-oxide (DMPO) and 4-oxo-2,2,6,6-tetramethylpiperidine (TEMP) were applied as the spin-trapping agent. The total organic carbon (TOC) concentration in the reaction solution was analyzed by a TOC analyzer (Shimadzu, TOC-VCPH) after passing through a 0.22 μm filter. The leaching capacity of Mn ions was measured by using an inductively coupled plasma-optical emission spectrometry (ICP-OES, PerkinElmer Optima 5300DV).

### 2.3. Degradation procedures

The photo-Fenton-like catalytic activity of the prepared mesoporous  $\text{MnO}_x$  microspheres was evaluated in the degradation of four typical fluoroquinolone antibiotics, i.e., OFL, CIP, ENR and LEV. The chemical structure of OFL, CIP, ENR and LEV is depicted in Fig. S1. The initial concentration of OFL, ENR and LEV were established for 30 μM, and 15 μM was determined for CIP based on their solubility. In a typical photo-Fenton degradation experiment, 0.1 g L<sup>-1</sup> catalyst was added into antibiotic solution with continuous stirring for 1 h to reach the adsorption-desorption equilibrium before switching to the light. The UV and simulated solar irradiation were produced by a 500 W mercury lamp (CEL-LAM500, 50 mW cm<sup>-2</sup>, maximum light intensity at 365 nm) and a 500 W xenon lamp (CEL-LAX500, wavelength range: 200–1000 nm, 100 mW cm<sup>-2</sup>) (Beijing China Education Au-light Co., Ltd), respectively. The photo-Fenton-like reaction simultaneously started when the 1 mM PMS was introduced under UV or simulated sunlight irradiation. At predetermined intervals, 1 mL aliquots were taken, centrifuged and filtered, then determined the concentration of antibiotic using Shimadzu UV-2600 spectrophotometer and high performance liquid chromatography (HPLC, Shimadzu LC-20 A). The transformation intermediates of CIP were analyzed by a LC-MS system (Thermo Scientific LCQ Fleet LC-MS). The details of the analytical methods of HPLC and LC-MS were supplied in SI. The catalytic stability of  $\text{Mn}_3\text{O}_4$  was studied by performing recycling test. After the reaction, the spent catalyst was collected via centrifugation, washed with DI water, and then dried at 100 °C for 6 h under the air environment. The residue was further employed for the photo-Fenton degradation of the antibiotic solution.

## 3. Results and discussion

### 3.1. Controllable synthesis of mesoporous $\text{MnO}_x$ microsphere

The diagram of the controllable synthesis of mesoporous  $\text{MnO}_x$  microspheres is illustrated in Fig. 1. As our previous studies [34,35] demonstrated that tri-block copolymer P123 surfactant could greatly promote the strong interaction of P123 template with the molecules, atoms and metal ions, resulting in a more homogeneous and rapid heat-up process (Fig. 1, a–c). The  $\text{MnO}_x$  core will be generated in the self-assemble step along the P123 micelles, and the growth step occurred in the hydrothermal treatment step (Fig. 1, d). Finally, the P123 template was removed via annealing treatment, and meanwhile the well-knit  $\text{MnO}_x$  microspheres were produced (Fig. 1, e).

XRD patterns were firstly employed to investigate the crystalline

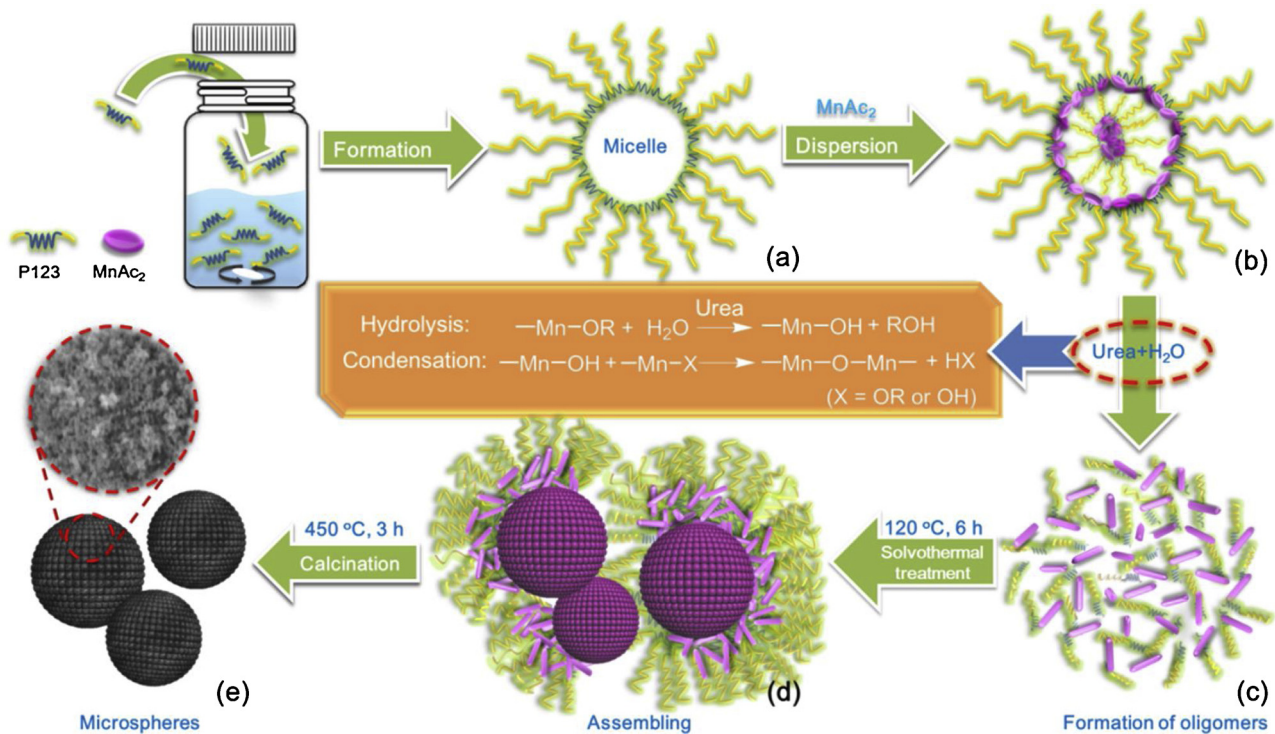


Fig. 1. Schematic illustration for the synthesis of mesoporous  $\text{MnO}_x$  microspheres.

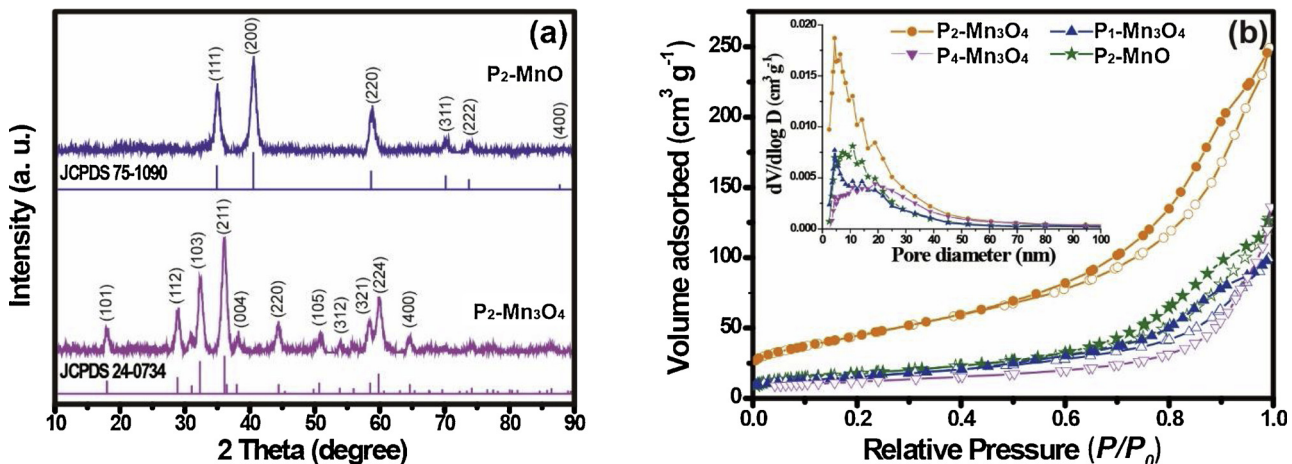
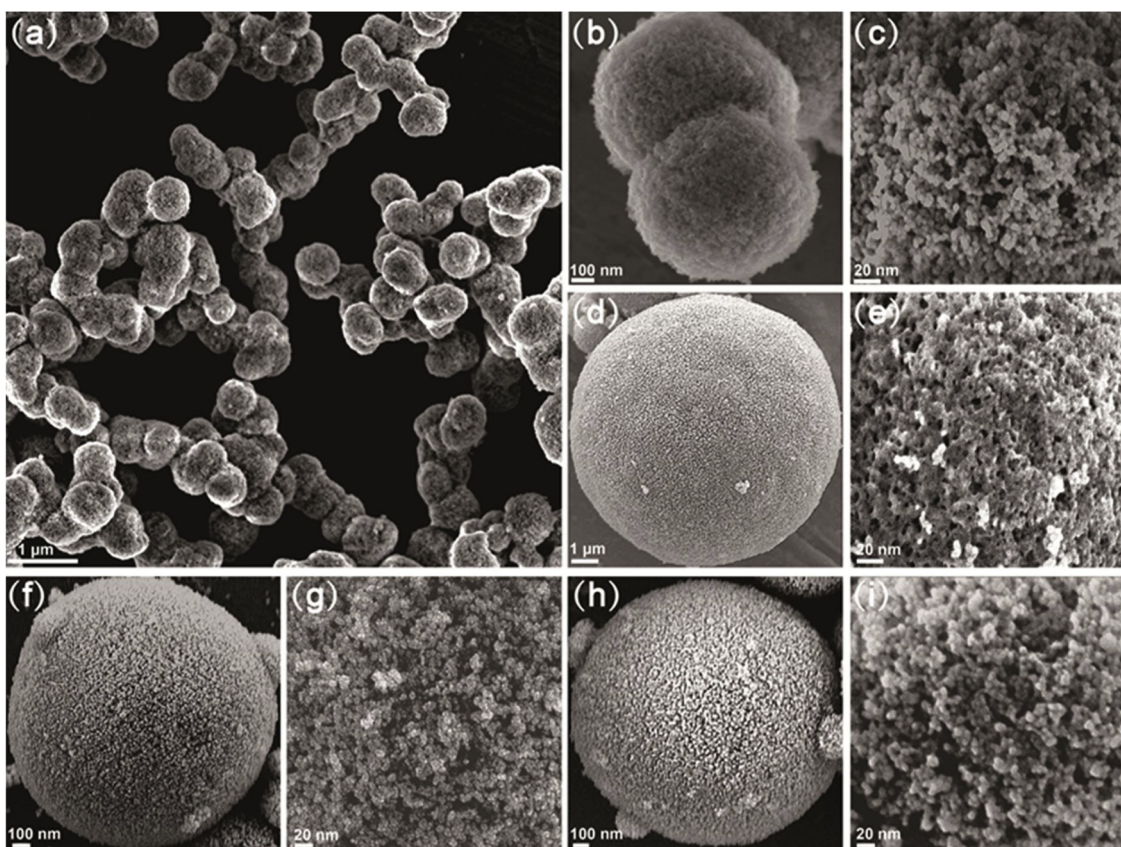


Fig. 2. (a) XRD patterns of the prepared  $\text{P}_2\text{-MnO}$  and  $\text{P}_2\text{-Mn}_3\text{O}_4$  photo-Fenton-like catalysts; (b) Nitrogen adsorption-desorption isotherms of  $\text{P}_2\text{-MnO}$ ,  $\text{P}_1\text{-Mn}_3\text{O}_4$ ,  $\text{P}_2\text{-Mn}_3\text{O}_4$  and  $\text{P}_4\text{-Mn}_3\text{O}_4$ . The inset shows the corresponding pore-size distribution plots of  $\text{P}_2\text{-MnO}$ ,  $\text{P}_1\text{-Mn}_3\text{O}_4$ ,  $\text{P}_2\text{-Mn}_3\text{O}_4$  and  $\text{P}_4\text{-Mn}_3\text{O}_4$ .

phase and structure as shown in Fig. 2a. It is very interesting to note that porous  $\text{MnO}$  microsphere will be obtained when the obtained gel was calcined under Ar, while porous  $\text{Mn}_3\text{O}_4$  microsphere will be achieved if the gel was treated in air. The diffraction peaks for the  $\text{P}_2\text{-Mn}_3\text{O}_4$  sample can be exclusively assigned to tetragonal-phase  $\text{Mn}_3\text{O}_4$  structure (JCPDS No.24-0734), and no distinct impurity phase was detected, implying that a high pure sample was successfully fabricated. For the  $\text{P}_2\text{-MnO}$  sample, the diffraction peaks are well coincident with the standard XRD pattern of  $\text{MnO}$  (JCPDS No.75-1090). The well-defined peaks appeared at  $2\theta$  angles of 34.9°, 40.6°, 58.7°, 70.2°, 73.8° and 87.7° are indexed to (111), (200), (311), (222) and (400) reflections of cubic-phase  $\text{MnO}$  structure. Again, no other characteristic reflections corresponding to impurities were found. Moreover, the mean size of  $\text{Mn}_3\text{O}_4$  and  $\text{MnO}$  nanocrystallites were calculated based on the Scherrer Equation to be 9.4 and 8.8 nm, respectively. In addition,  $\text{P}_0\text{-Mn}_3\text{O}_4$ ,  $\text{P}_1\text{-Mn}_3\text{O}_4$ ,  $\text{P}_4\text{-Mn}_3\text{O}_4$ ,  $\text{P}_0\text{-MnO}$ ,  $\text{P}_1\text{-MnO}$  and  $\text{P}_4\text{-MnO}$  samples

were also analyzed by XRD (Fig. S2), and the diffraction peaks are unambiguously indexed to  $\text{Mn}_3\text{O}_4$  and  $\text{MnO}$  phase with high crystallinity, respectively.

The BET specific surface area and pore size distribution of the synthesized  $\text{P}_2\text{-MnO}$ ,  $\text{P}_1\text{-Mn}_3\text{O}_4$ ,  $\text{P}_2\text{-Mn}_3\text{O}_4$  and  $\text{P}_4\text{-Mn}_3\text{O}_4$  spherical catalysts are further analyzed by  $\text{N}_2$  adsorption-desorption test. From the adsorption-desorption isotherms (Fig. 2b and Fig. S3), all catalysts displayed a type-IV isotherm with H3 hysteresis loop at a relative pressure ( $P/P_0$ ) ranges of 0.6–0.95, suggesting the existence of mesopores [36]. The values of the specific surface area, pore volume and pore size are summarized in Table S1. The specific surface area of  $\text{P}_2\text{-Mn}_3\text{O}_4$  was significantly higher than those of  $\text{P}_1\text{-Mn}_3\text{O}_4$ , and  $\text{P}_4\text{-Mn}_3\text{O}_4$ , showing 2 g P123 was better for the formation of  $\text{Mn}_3\text{O}_4$  microsphere. The large surface area and mesoporous structure would be beneficial for the enhanced adsorption of antibiotic molecules and facilitation of the activating PMS to form highly active oxidants, leading to the



**Fig. 3.** SEM images of the synthesized  $\text{Mn}_3\text{O}_4$  and  $\text{MnO}$  photo-Fenton-like catalysts with various amount of P123 and under different calcining atmosphere: (a–c)  $\text{P}_1\text{-Mn}_3\text{O}_4$ ; (d and e)  $\text{P}_4\text{-Mn}_3\text{O}_4$ ; (f–g)  $\text{P}_2\text{-Mn}_3\text{O}_4$ ; (h–i)  $\text{P}_2\text{-MnO}$ .

efficient removal of antibiotics.

As shown in Fig. 3a–c, SEM images of the prepared  $\text{P}_1\text{-Mn}_3\text{O}_4$  presented a typical sphere-like morphology with high uniform dispersion. The diameters of microspheres increased with the amount of the P123 surfactant, where  $\text{P}_1\text{-Mn}_3\text{O}_4$ ,  $\text{P}_2\text{-Mn}_3\text{O}_4$  and  $\text{P}_4\text{-Mn}_3\text{O}_4$  were of  $0.65 \pm 0.5 \mu\text{m}$  (Fig. 3b),  $2.45 \pm 1.0 \mu\text{m}$  (Fig. 3f) and  $4.50 \pm 1.0 \mu\text{m}$  (Fig. 3d), respectively. Besides, these microspheres were compactly stacked by tiny  $\text{Mn}_3\text{O}_4$  nanoparticles to form mesoporous structures. However, when the  $\text{Mn}_3\text{O}_4$  microsphere was synthesized using 4 g P123, the porous structure existed on the catalyst surface is not obvious, and SEM image (Fig. 3e) shows that it is consisted of much bigger  $\text{Mn}_3\text{O}_4$  particles, leading to the clear aggregation. Thus, 2.0 g P123 was chosen for the further study on the  $\text{MnO}_x$  microsphere. In comparison, the different calcining atmosphere (air or Ar) has little influence on the texture and size of resulting porous spherical materials. For example,  $\text{P}_2\text{-Mn}_3\text{O}_4$  (Fig. 3, f and g) synthesized using 2 g P123 and then calcined under air, shows similar pore size and morphology as  $\text{P}_2\text{-MnO}$  (Fig. 3, h and i) prepared by 2 g P123 and then calcined under Ar. The elemental mapping of  $\text{P}_2\text{-Mn}_3\text{O}_4$  (Fig. S4) displays homogeneous distribution of Mn and O throughout the  $\text{Mn}_3\text{O}_4$  microsphere, and the EDX spectrum (Fig. S5) further confirms the peaks of Mn and O where they should be. In addition, the morphology of  $\text{P}_0\text{-Mn}_3\text{O}_4$  and commercial  $\text{MnO}_x$  is also analyzed for comparison, as shown in Fig. S6, no regular sphere was observed for these materials. In summary, the template P123 exhibited the crucial role in the controllable synthesis of mesoporous  $\text{MnO}_x$  microspheres.

TEM was further used to study the representative  $\text{P}_2\text{-Mn}_3\text{O}_4$  and  $\text{P}_2\text{-MnO}$  microspheres. TEM images of the as-made  $\text{P}_2\text{-Mn}_3\text{O}_4$  (Fig. 4a and b) reveal that the subunits of these porous microspheres are made up of small size nanoparticles, which were in the range of 9–15 nm. The selected area electron diffraction (SAED) analysis (Inset in Fig. 4b) indicates polycrystalline feature across the entire tetragonal-phase  $\text{P}_2$

$\text{Mn}_3\text{O}_4$  microspheres, and lattice fringes with 0.277, 0.309 and 0.492 nm space can be observed clearly in high-resolution (HR) TEM image (Fig. 4c), which are well coincident with the (103), (112) and (101) plane of hausmannite  $\text{Mn}_3\text{O}_4$ . For the  $\text{P}_2\text{-MnO}$  catalyst, TEM images (Fig. 4, d and e) present that the subunits of  $\text{MnO}$  microspheres are composed of relatively smaller nanoparticles ( $\sim 8 \text{ nm}$ ), whereas these particles are more condensed. Furthermore, the SAED pattern (Inset in Fig. 4e) demonstrates polycrystalline feature of cubic  $\text{MnO}$ , and HR-TEM image exhibits well-resolved lattice fringes with spacings of 0.134, 0.222 and 0.256 nm, corresponding to the (311), (200) and (111) plane of manganosite  $\text{MnO}$  (Fig. 4f). The crystalline structures of  $\text{P}_2\text{-Mn}_3\text{O}_4$  and  $\text{P}_2\text{-MnO}$  materials obtained from HR-TEM are well matched with XRD results. Overall, the fluffy and porous surface of  $\text{P}_2\text{-Mn}_3\text{O}_4$  catalyst was comprised by a large number of tiny  $\text{Mn}_3\text{O}_4$  nanoparticles, which was expected to provide more reactive centers and adsorption sites to accelerate the degradation of antibiotics.

### 3.2. Antibiotics degradation

The photo-Fenton-like performances of the as-prepared  $\text{MnO}_x$  microspheres were investigated using four typical FQs antibiotics. The time-dependent decomposition profile of OFL is presented in Fig. 5a. Obviously, the OFL was fairly stable in the blank test, confirming its self-degradation could be negligible. The treatment of OFL using UV irradiation, PMS/UV and  $\text{P}_2\text{-Mn}_3\text{O}_4$ /PMS/dark systems were found to result in a sluggish degradation. The synthesized mesoporous  $\text{MnO}/\text{Mn}_3\text{O}_4$  microspheres presented the superior activity for the elimination of OFL, and 89.3%, 93.2%, and 95.4% of removal efficiencies were observed for the  $\text{P}_1\text{-Mn}_3\text{O}_4$ ,  $\text{P}_2\text{-MnO}$ , and  $\text{P}_4\text{-Mn}_3\text{O}_4$  samples assisted by PMS under UV irradiation, respectively. More interesting, the  $\text{P}_2\text{-Mn}_3\text{O}_4$  catalyst manifested the optimal reactivity and adsorption performance, and 99.5% OFL degradation was achieved, which was 2.1 times higher

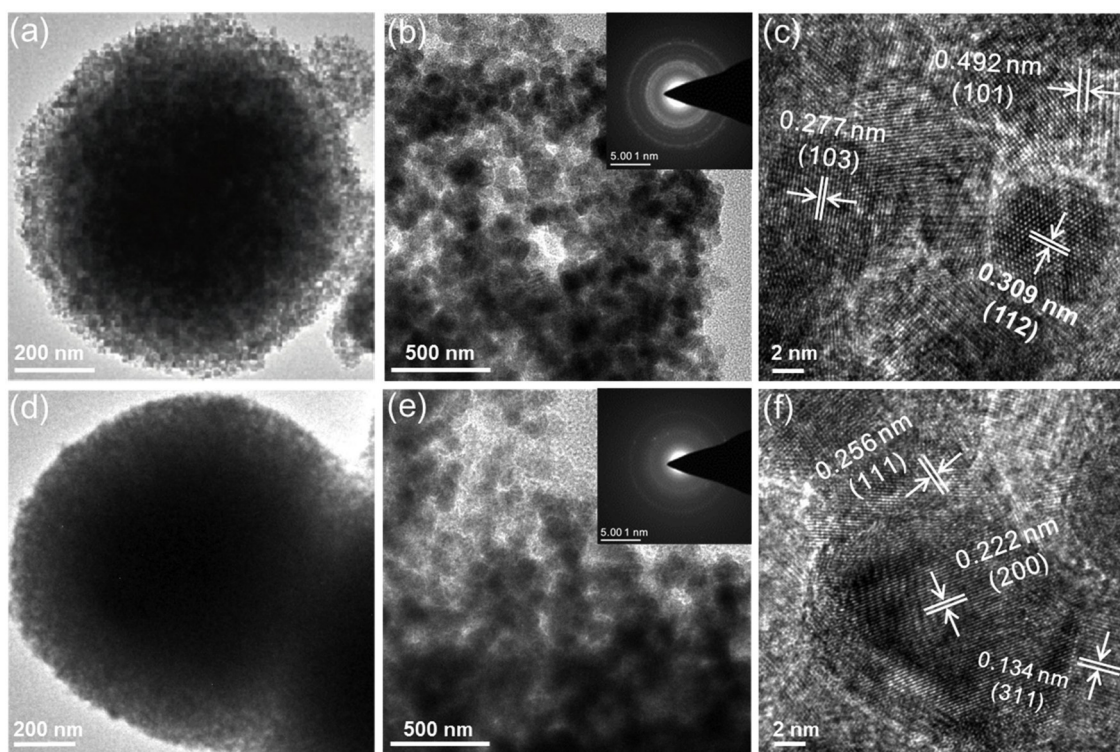


**Fig. 4.** TEM and HR-TEM images of the prepared (a–c)  $\text{P}_2\text{-Mn}_3\text{O}_4$  and (d–f)  $\text{P}_2\text{-MnO}$  photo-Fenton-like catalysts with inset of SAED analysis.

than that of the commercial Mn oxide (abbreviated as C-Mn oxide). These results demonstrated that the mesoporous structure of  $\text{P}_2\text{-Mn}_3\text{O}_4$  microsphere could offer more reactive centers and adsorption sites available for PMS and antibiotic molecules, giving rise to the stronger absorption property and robust catalytic behavior.

In the present work, the pseudo-first-order kinetics model ( $\ln(C/C_0) = -k_{obs} \cdot t$ , where  $C_0$  is the initial concentration of antibiotics (M);  $C$  is the antibiotics concentration ( $\mu\text{ M}$ ) at a given length of time  $t$  (min); and  $k_{obs}$  denotes the degradation rate constant ( $\text{min}^{-1}$ )) is used to investigate the degradation of OFL on various catalysts assisted with PMS after 5 min of UV irradiation (Fig. 5b). The correlation coefficient ( $R^2 \geq 0.99$ ) indicated that the degradation process could be generally described by the pseudo-first-order kinetics model. It was clearly noting that the  $\text{P}_2\text{-Mn}_3\text{O}_4/\text{PMS}/\text{UV}$  system demonstrated the highest  $k_{obs}$  value ( $0.667 \text{ min}^{-1}$ ), which was 2.4 and 5.6 times higher than those in  $\text{P}_0\text{-Mn}_3\text{O}_4/\text{PMS}/\text{UV}$  and C-Mn oxide/PMS/UV systems, respectively. These results revealed that the mesoporous structure of  $\text{P}_2\text{-Mn}_3\text{O}_4$  microsphere catalyst had excellent activity for the activation of PMS, which could promote the antibiotics degradation with high efficiency.

The simulated sunlight driven photo-Fenton-like catalytic degradations of FQs antibiotics on the  $\text{P}_2\text{-Mn}_3\text{O}_4$  catalyst were also investigated. In Fig. 5c, the removal efficiencies of FQs antibiotics and TOC in the  $\text{P}_2\text{-Mn}_3\text{O}_4/\text{PMS}/\text{UV}$  system and the  $\text{P}_2\text{-Mn}_3\text{O}_4/\text{PMS}/\text{simulated sunlight}$  system are presented. The self-photolysis showed a degradation of less than 10.3% of the initial concentration after 10 min under irradiation (Fig. S7). When both catalyst and PMS were applied in antibiotic solution, remarkably enhanced degradation efficiencies could be observed. Approximate 74.5% of OFL, 79.4% of CIP, 72.3% of ENR and 81.9% of LEV were degraded by  $\text{P}_2\text{-Mn}_3\text{O}_4$  under simulated sunlight irradiation for just 10 min in the presence of PMS. Besides, under UV irradiation, the as-prepared  $\text{P}_2\text{-Mn}_3\text{O}_4$  coupled with PMS could remove 99.5% of OFL, 97.8% of CIP, 99.1% of ENR and 98.5% of LEV in 10 min respectively. The above results indicated that the novel heterogeneous photo-Fenton-like system could make the most of UV and visible light of the solar spectrum in the catalytic oxidation process. Furthermore, TOC removal efficiencies were used to determine the mineralization degree

of antibiotics in the solution. These FQs antibiotics were effectively mineralized by the  $\text{P}_2\text{-Mn}_3\text{O}_4$  catalyst combined with PMS after 10 min of UV or simulated sunlight irradiation, suggesting that partial intermediates could be mineralized during the photo-Fenton-like reaction.

The stability of  $\text{P}_2\text{-Mn}_3\text{O}_4$  was further evaluated through recycling the catalyst toward photo-Fenton-like degradation of OFL, CIP, ENR and LEV under UV irradiation. As described in Fig. 5d, the higher degradation efficiencies of OFL (87.6%), CIP (84.7%), ENR (82.3%) and LEV (88.5%) still can be achieved on the  $\text{P}_2\text{-Mn}_3\text{O}_4$  catalyst over three successive runs, indicating its attractive stability. The slight decline in catalytic activity might be attributed to the passivation of catalyst surface caused by remaining antibiotics/intermediates, or the loss of catalyst during the recycling process. Noticeably, slight leaching of Mn ions ( $1.59, 1.20, 1.78$  and  $1.31 \text{ mg L}^{-1}$ ) were detected by ICP-OES after three cycles of OFL, CIP, ENR and LEV degradation, avoiding the formation of manganese enriched sludge. Moreover, the main characteristic reflections in the XRD pattern of spent catalyst (Fig. S8) can be well assigned to the  $\text{Mn}_3\text{O}_4$  phase, suggesting the high structural stability.

To further evaluate the potential of the  $\text{P}_2\text{-Mn}_3\text{O}_4/\text{PMS}/\text{UV}$  system for the remediation of FQs-contaminated water body, the photo-Fenton-like catalytic degradation of OFL, CIP, ENR and LEV were investigated. The change in the UV-vis spectra of four widely used FQs antibiotics with reaction time is illustrated in Fig. 6. As the photo-Fenton-like reaction proceeding, the characteristic absorption peaks of OFL, CIP, ENR and LEV appeared at 287, 271, 271 and 287 nm rapidly disappeared. These data confirmed that the molecular structure of these antibiotics were gradually destroyed by some reactive oxygen species (ROS) and completely decomposed by the  $\text{P}_2\text{-Mn}_3\text{O}_4/\text{PMS}/\text{UV}$  system within or less than 10 min. In addition, the best adsorption efficiency of  $\text{P}_2\text{-Mn}_3\text{O}_4$  could reach up to 15.6% for CIP. To benchmark our catalyst, we compared the catalytic performance with other preciously studied materials from literatures in Table S2, the  $\text{P}_2\text{-Mn}_3\text{O}_4$  catalyst presented a much higher activity for the removal of antibiotics.

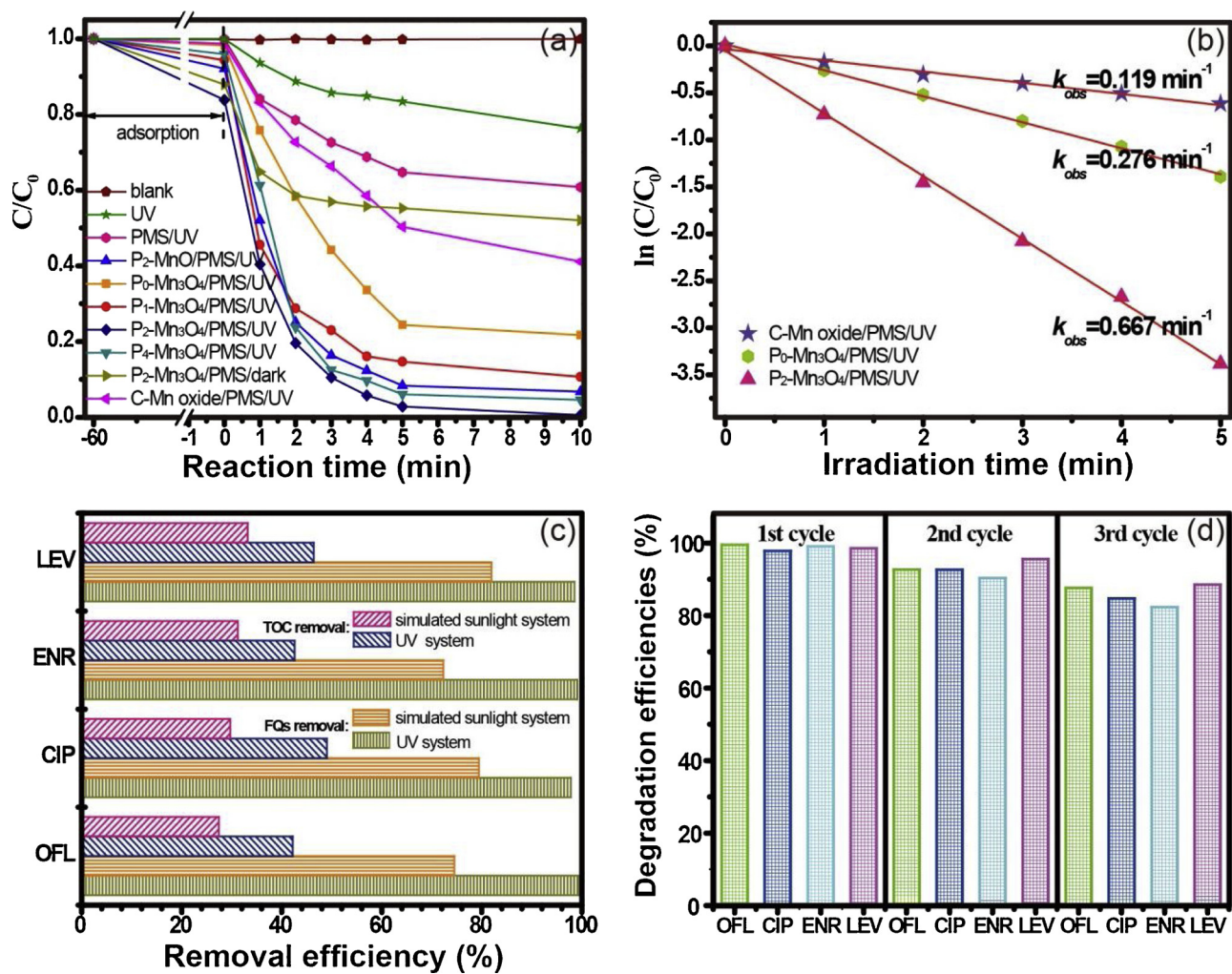


**Fig. 5.** (a) Comparison of the photo-Fenton-like catalytic efficiencies of different systems. (b) The pseudo-first-order kinetic plots for the degradation of OFL. (c) The FQs antibiotics and TOC removal efficiencies in the  $P_2\text{-Mn}_3\text{O}_4/\text{PMS}/\text{UV}$  system and the  $P_2\text{-Mn}_3\text{O}_4/\text{PMS}/\text{simulated sunlight}$  system. (d) Recycling performances of  $P_2\text{-Mn}_3\text{O}_4$  toward OFL, CIP, ENR and LEV degradation using PMS as the oxidant under UV irradiation. Reaction conditions are as follows: 0.1 g L<sup>-1</sup>  $P_2\text{-Mn}_3\text{O}_4$ , 1 mM PMS, 30  $\mu\text{M}$  (OFL or ENR or LEV), 15  $\mu\text{M}$  CIP, pH = 7, 25 °C, and reaction time of 10 min.

### 3.3. Degradation pathways

The degraded intermediates of CIP during the photo-Fenton-like process were identified by liquid chromatography-mass spectrometry (LC-MS). The details of these intermediates are summarized in Table S3, and the MS spectra are shown in Fig. S9. Based on the identified intermediates, three major reaction pathways involved in CIP degradation were proposed in Fig. 7.

The first pathway is proposed as following and the transformation process was similar to the results demonstrated in previous reports [7,37]. The CIP degradation was initiated by the cleavage of the piperazine ring. The piperazine ring was firstly broken to give  $m/z$  362, and then transferred into  $m/z$  334 via loss of  $-\text{CO}$  group. The second  $-\text{CO}$  group was eliminated resulting in the formation of  $m/z$  306. In the last step,  $m/z$  263 could be produced through further oxidation of the compound  $m/z$  306, leading to the total destruction of the piperazinyl substituent.

The second possible pathway involves defluorination, oxidation of quinolone and benzene rings, as well as the loss of the piperazine moiety. The C=C of quinolone group was the most likely reaction center to be attacked by ROS [38,39]. Accordingly, CIP underwent an OH/F substitution and oxidation step to open the quinolone ring, giving rise to  $m/z$  362. After that, through detachment of the  $-\text{CO}$  unit, the product of  $m/z$  334 was formed. Ultimately, the product  $m/z$  256 was

produced via further benzene ring oxidation and the loss of the piperazine moiety to completely destroy the CIP structure.

The third pathway is mainly assigned to the hydroxylation process. In this way, CIP was started by hydroxylation (Pathway 3a) to generate  $m/z$  348 or defluorination combined with hydroxylation (Pathway 3b) to produce  $m/z$  346. Further hydroxylation led to the formation of  $m/z$  334. Then, the subsequent reaction would lead to the cleavage of the quinolone ring, which produced the  $m/z$  334 [40,41]. In fact, the hydroxylation process of CIP has also been proposed in previous literatures [39]. Additionally, according to the TOC analysis, these by-products could be further decomposed to realize the complete mineralization in the  $P_2\text{-Mn}_3\text{O}_4/\text{PMS}/\text{UV}$  system.

### 3.4. Mechanism study

To compare the chemical states between the fresh and spent  $P_2\text{-Mn}_3\text{O}_4$  catalyst, XPS were performed. As shown in Fig. 8a, XPS survey clearly confirms the existence of Mn and O in the sample. The Mn 2p core-level region (Fig. 8b) shows the peaks appeared at 641.9 and 653.4 eV are assigned to Mn 2p<sub>3/2</sub> and Mn 2p<sub>1/2</sub> confirming the generation of  $\text{Mn}_3\text{O}_4$ . More specifically, the asymmetrical Mn 2p<sub>3/2</sub> signal of the fresh  $P_2\text{-Mn}_3\text{O}_4$  composed of two separate peaks centered at 641.6 and 643.4 eV, which could be corresponding to  $\text{Mn}^{3+}$  and  $\text{Mn}^{2+}$  covalent, respectively [42]. Based on the peak fitting of O 1s spectrum

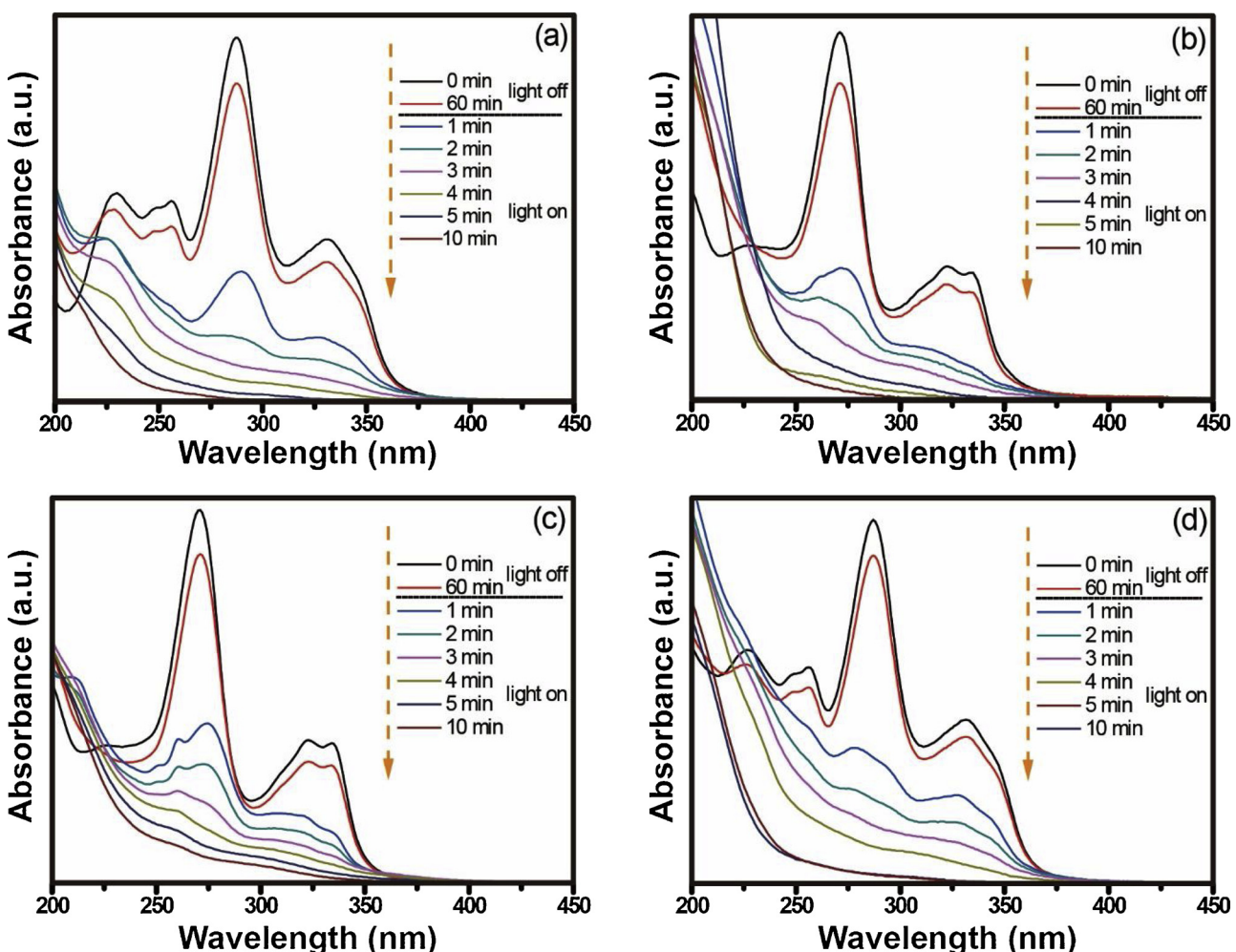


**Fig. 6.** Change in the UV-vis spectra, with time, during the photo-Fenton-like reaction of the (a) OFL, (b) CIP, (c) ENR and (d) LEV solution in the P<sub>2</sub>-Mn<sub>3</sub>O<sub>4</sub>/PMS/UV system. Reaction conditions are as follows: 0.1 g L<sup>-1</sup> P<sub>2</sub>-Mn<sub>3</sub>O<sub>4</sub>, 1 mM PMS, 30 μM (OFL or ENR or LEV), 15 μM CIP, pH = 7, 25 °C, and reaction time of 10 min.

(Fig. S10), three apparent peaks located at 530.0, 531.1 and 533.2 eV can be detected, which could be ascribed to lattice oxygen species with metal or surface hydroxyl groups [29,30]. Besides, the P<sub>2</sub>-MnO sample was also studied by XPS as shown in Fig. S11. The binding energies at 641.4 eV for Mn 2p<sub>3/2</sub> and 653.1 eV for Mn 2p<sub>1/2</sub> indicated the existence of Mn<sup>2+</sup> [43].

After the photo-Fenton-like degradation of antibiotics, XPS shows the Mn 2p<sub>3/2</sub> peak shifted slightly toward a higher binding energy (642.5 eV), which can be well fitted into three peaks, Mn<sup>3+</sup> (641.7 eV), Mn<sup>4+</sup> (642.5 eV) and Mn<sup>2+</sup> (643.4 eV), respectively. In comparison, the relative atomic percentages of Mn<sup>2+</sup>, Mn<sup>3+</sup> and Mn<sup>4+</sup> were 35.7%, 21.8% and 42.5% for the spent catalyst, and the fresh P<sub>2</sub>-Mn<sub>3</sub>O<sub>4</sub> sample contained 33.5% Mn<sup>2+</sup> and 66.5% Mn<sup>3+</sup>. These results documented that the inter-conversions between Mn ions on the catalyst surface occurred during the redox reaction, resulting in the continuous activation of PMS for the faster removal of antibiotics. Interestingly, in the case of the spent catalyst, the relative content of surface •OH component/adsorbed O<sub>2</sub> was observed to be reduced from 32.7% to 27.0%, while the percentage of adsorbed H<sub>2</sub>O increased, indicating that oxygen species might be involved in the process.

Several highly ROS like sulfate radical (SO<sub>4</sub><sup>•-</sup>), hydroxyl radical (•OH), superoxide radical (O<sub>2</sub><sup>•-</sup>) and singlet oxygen (<sup>1</sup>O<sub>2</sub>) were *in-situ* responsible for the decomposition of antibiotics. To understand the nature of the primary free radicals involved in the P<sub>2</sub>-Mn<sub>3</sub>O<sub>4</sub>/PMS/simulated sunlight and P<sub>2</sub>-Mn<sub>3</sub>O<sub>4</sub>/PMS/UV systems during FQs antibiotics degradation, ESR analysis were carried out with DMPO and

TEMP as the spin-trapping agent. As illustrated in Fig. 9a, in the presence of PMS, the signals of DMPO-•OH and DMPO-SO<sub>4</sub><sup>•-</sup> were easily detected in the suspension of P<sub>2</sub>-Mn<sub>3</sub>O<sub>4</sub> under UV or simulated sunlight irradiation, indicating the existence of •OH and SO<sub>4</sub><sup>•-</sup> radicals during the photo-Fenton-like reaction. However, compared with the reaction under UV light, the •OH/SO<sub>4</sub><sup>•-</sup> signals were relatively weakened in the P<sub>2</sub>-Mn<sub>3</sub>O<sub>4</sub>/PMS/simulated sunlight system. This is mainly because that the light wavelength has influence on the activation of PMS. The short-wavelength irradiation has higher energy than long-wavelength to activate PMS, effectively breaking the O–O bond of PMS to form SO<sub>4</sub><sup>•-</sup> [24,44]. Similarly, the characteristic signals of DMPO-O<sub>2</sub><sup>•-</sup> and TEMP-<sup>1</sup>O<sub>2</sub> were more strong in the UV light driven photo-Fenton-like system (Fig. 9, b and c), which could be attributed to the following aspects: (1) the mesoporous structure of MnO<sub>x</sub> microsphere would enhance the mass transportation of reactant and intermediate, and accelerate the reaction rate under UV light irradiation; (2) UV irradiation could induce the photo-reduction of Mn ions on the surface of manganese oxide from high valence to low valence which in reverse reacted with PMS. Thus redox cycles of Mn ions on the surface of manganese oxide could be promoted under UV light. These results confirmed that more ROS, especially the O<sub>2</sub><sup>•-</sup> and <sup>1</sup>O<sub>2</sub>, would be generated in the P<sub>2</sub>-Mn<sub>3</sub>O<sub>4</sub>/PMS/UV system, leading to the superior performance. Besides, as displayed in Fig. 9d, the ESR signals at g of 2.004 were corresponded to the oxygen vacancies on the irradiated P<sub>2</sub>-Mn<sub>3</sub>O<sub>4</sub> surface as electron-trapping centers, revealing the existence of photoexcited electrons (e<sup>-</sup>) and holes (h<sup>+</sup>) [45,46]. In the PMS alone system, no obvious ESR signal

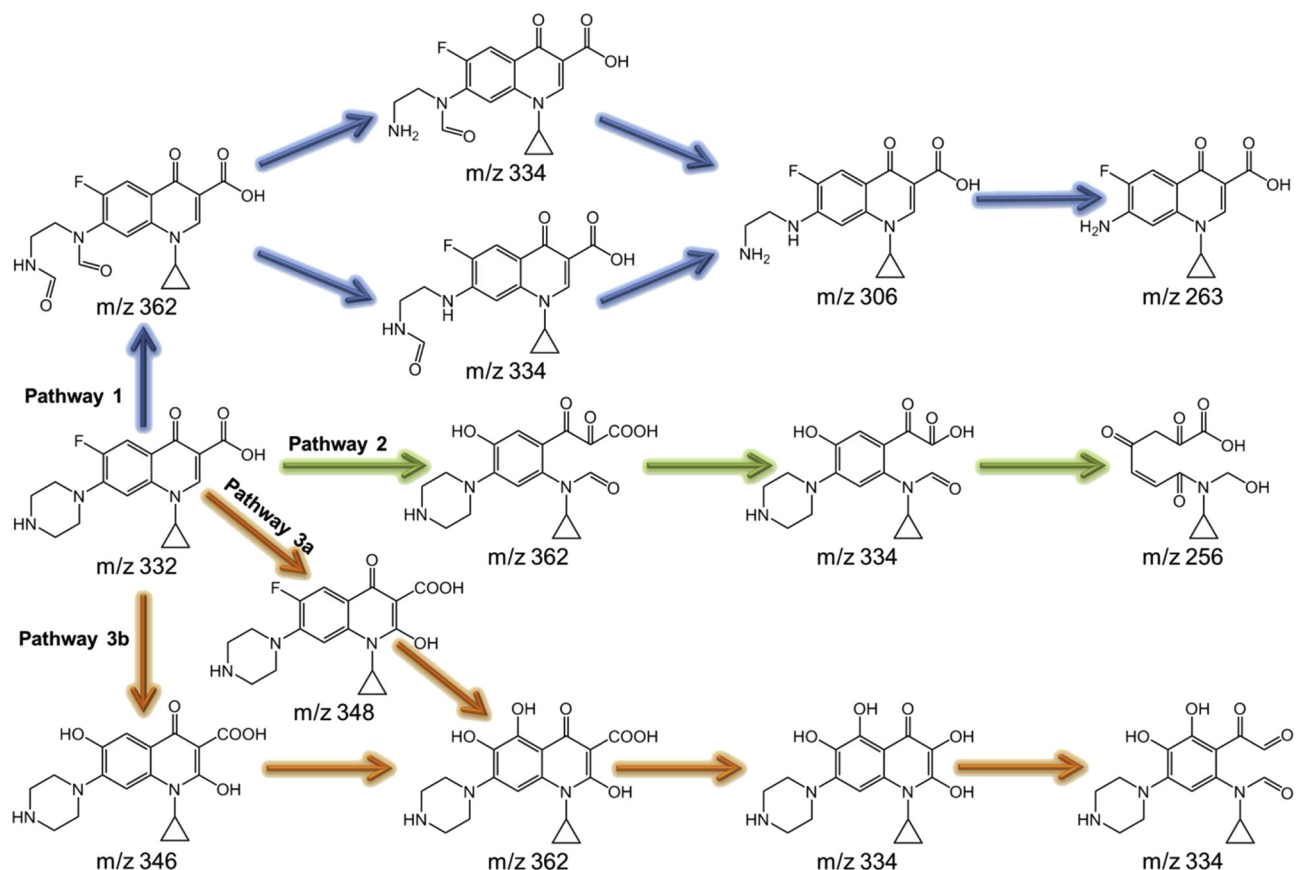


Fig. 7. Proposed degradation pathways for CIP degradation in the  $P_2\text{-Mn}_3\text{O}_4/\text{PMS}/\text{UV}$  system.

of these radicals could be found (Fig. S12), indicating the important role of  $P_2\text{-Mn}_3\text{O}_4$  catalyst and light irradiation in the photo-Fenton-like system.

Based on above investigations, a rational heterogeneous photo-Fenton-like reaction mechanism on the mesoporous  $\text{Mn}_3\text{O}_4$  microsphere was proposed in Fig. 10. The rapid diffusion of antibiotic molecules toward the  $\text{Mn}_3\text{O}_4$  surface and then being absorbed on the reactive sites was the first step for the degradation reaction. Subsequently, the oxidative decomposition of antibiotics occurred, which was induced by nascent ROS with strong reactivity mainly resulted from the activation process of PMS. In this step, various oxidation-reduction reactions involved individually or simultaneously. In

detail, PMS could initially accept one electron via the oxidation of  $\equiv \text{Mn}^{\text{II}}/\equiv \text{Mn}^{\text{III}}$ , producing surface-bound  $\text{SO}_4^{\cdot-}$  (Eqs. (1) and (2)) [42]. On the other hand, partial  $\equiv \text{Mn}^{\text{II}}$  could be regenerated from the reduction of the  $\equiv \text{Mn}^{\text{III}}$  by PMS, with the generation of  $\text{SO}_5^{\cdot-}$  (Eq. (3)), which was thermodynamically favorable because the standard reduction potential of  $\text{HSO}_5^{\cdot-}/\text{SO}_5^{\cdot-}$  ( $E^\circ = 1.1 \text{ V}$ ) was lower than that of  $\text{Mn}^{3+}/\text{Mn}^{2+}$  ( $E^\circ = 1.51 \text{ V}$ ) [47]. Then, a portion of  $\text{SO}_4^{\cdot-}$  could be transformed into  $\cdot\text{OH}$  through reaction with  $\text{H}_2\text{O}/\text{OH}^-$  (Eqs. (4) and (5)). Based on XPS and ESR analysis, as well as previous literature [48–50], we speculated that the electrons offered by  $\text{Mn}_3\text{O}_4$  could also be captured by  $\text{O}_2$  to form  $\text{H}_2\text{O}_2$  (Eqs. (6) and (7)), and eventually it might be decomposed into  $\cdot\text{OH}$  (Eq. (8)) or react with  $\cdot\text{OH}$  to generate

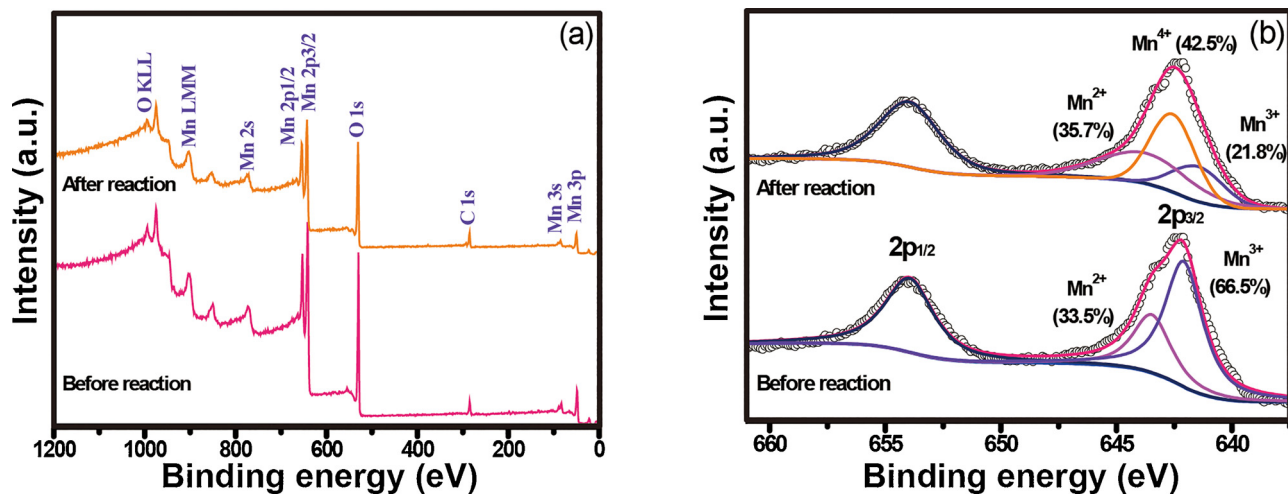
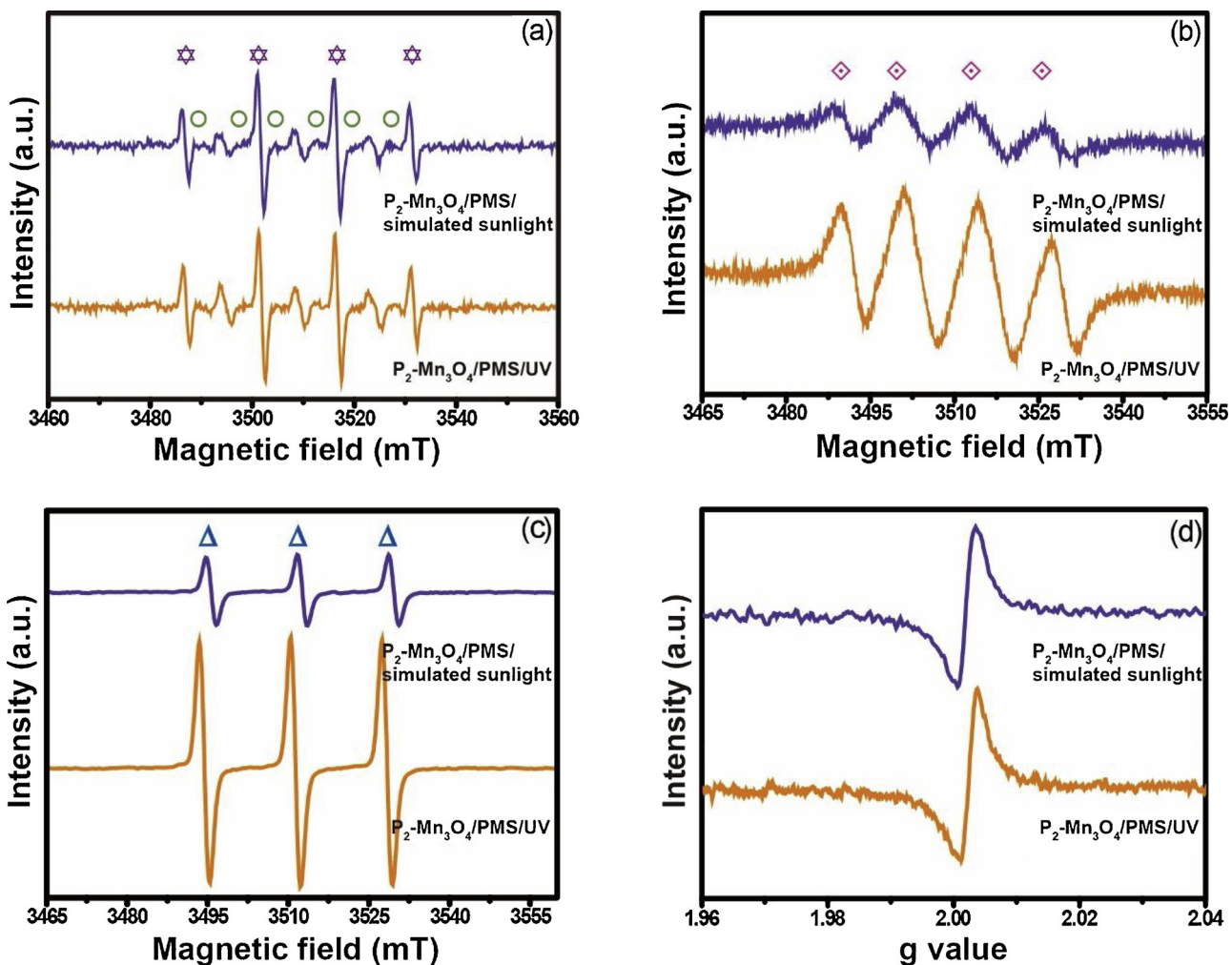
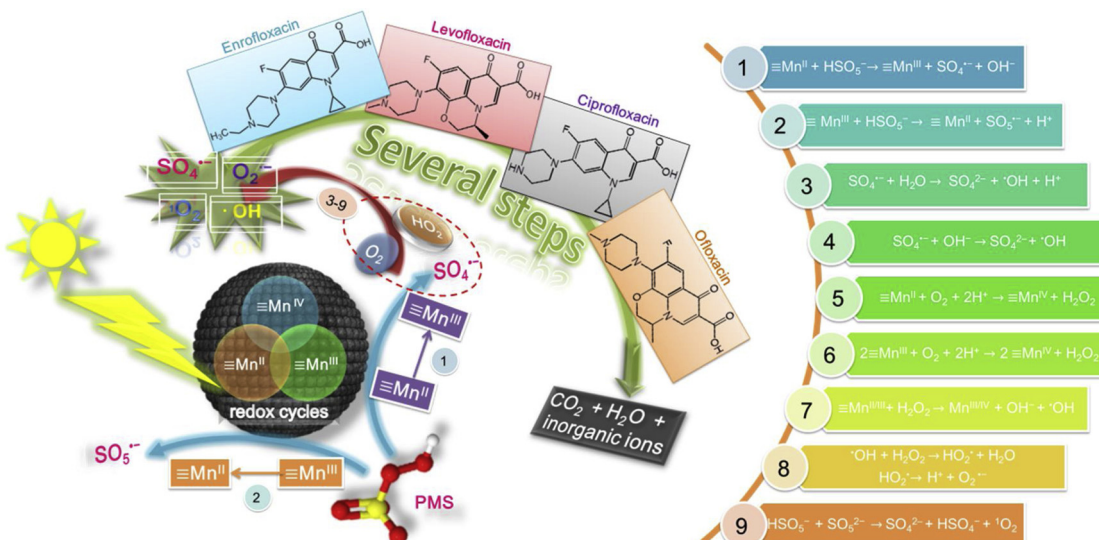


Fig. 8. (a) XPS survey and (b) Mn 2p spectra of  $P_2\text{-Mn}_3\text{O}_4$  photo-Fenton-like catalysts before and after reaction.

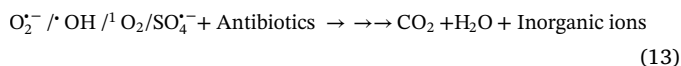
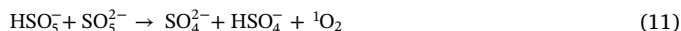
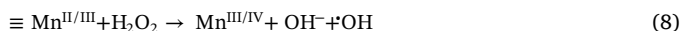
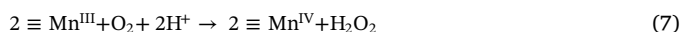
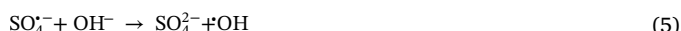
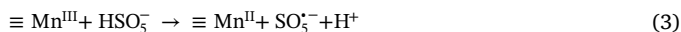
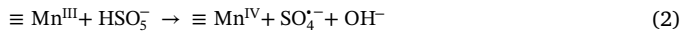
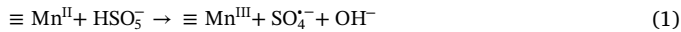


**Fig. 9.** ESR spectra of the (a) DMPO- $\text{SO}_4^{2-}$  (green circle), DMPO- $\cdot\text{OH}$  (purple star), (b) DMPO- $\text{O}_2^{\cdot-}$  (pink square), and (c) TEMP- $\text{O}_2^{\cdot-}$  adducts (blue triangle), recorded under UV and simulated sunlight irradiation. (d) ESR spectra of the  $\text{P}_2\text{-Mn}_3\text{O}_4$  catalyst under UV and simulated sunlight irradiation. Reaction conditions are as follows: 10 ppm DMPO, 10 ppm TEMP, 0.1 g L<sup>-1</sup>  $\text{P}_2\text{-Mn}_3\text{O}_4$ , 1 mM PMS, 30  $\mu\text{M}$  OFL, 25 °C, pH of 7, and reaction time of 5 min (For interpretation of the references to colour in this figure legend, the reader is referred to the web version of this article).



**Fig. 10.** Schematic illustration of the heterogeneous photo-Fenton-like reaction mechanism for the degradation of FQs antibiotics.

$O_2^{\cdot-}$  (Eqs.(9) and (10)). The production of  ${}^1O_2$  was correlated with the self-oxidation of PMS (Eq. (11)) [47]. The decomposition of PMS by light occurred to form  $SO_4^{\cdot-}$  and  $OH^{\cdot}$  via Eq. (12) [24]. In the meantime, the UV or simulated sunlight irradiation could not only facilitate the redox cycles of Mn ions on the  $Mn_3O_4$  surface [51], but also excite the  $Mn_3O_4$  materials to generate  $e^-$  and  $h^+$  (Fig. 9d), which then reacted with PMS to create active radicals [52,53], leading to further accelerate antibiotics degradation process. Lastly, the nonselective attack of the formed ROS generated various intermediates and small molecules like  $CO_2$  and  $H_2O$  (Eq. (13)), and the degradation products would be quickly desorbed off the reactive sites on the catalyst surface, and make them available for the following degradation reaction.



#### 4. Conclusions

The shape-controlled  $MnO_x$  microsphere with mesoporous structure was rationally designed and successfully synthesized. The amount of P123 surfactant and calcining atmosphere were found to play a vital role in the control of the morphology and crystalline phase of the prepared materials. The as-prepared  $P_2-Mn_3O_4$  sample exhibited the optimal catalytic activity on the activation of PMS, and it could remove 99.5% of OFL, 97.8% of CIP, 99.1% of ENR and 98.5% of LEV from aqueous solution in 10 min under UV irradiation, respectively. Besides, 74.5% of OFL, 79.4% of CIP, 72.3% of ENR and 81.9% of LEV were degraded on the  $P_2-Mn_3O_4$  catalyst with PMS under simulated sunlight irradiation for 10 min. Based on the LC-MS analysis, three major reaction pathways involved in CIP degradation were proposed, including the cleavage of quinolone and piperazine ring, defluorination and hydroxylation process.

This work documented an effective strategy for the removal of FQs antibiotics, and the superior photo-Fenton-like catalytic activity could be attributed to several striking features: (1) the controllable synthesis of  $MnO_x$  microsphere would provide more exposed reactive sites that were not only favorable for PMS activation to form ROS, but also helpful for the absorption of antibiotic molecules, leading to superior catalytic performances; (2) the mesoporous structure of  $MnO_x$  microsphere with large surface area, which dramatically enhanced the mass transportation; (3) both reactivity and structure of the  $MnO_x$  catalyst remained stable during the reaction; (4) reactive oxygen species could be sustainably and efficiently produced from PMS assisted with the redox cycles of Mn ions on the  $Mn_3O_4$  surface promoted by UV or simulated sunlight irradiation.

#### Acknowledgments

This work was supported by National Key R&D Program of China (2018YFD0800700), National Natural Science Foundation of China (21776324), Guangdong Provincial Key Laboratory of Environmental Pollution Control and Remediation Technology (2018K02), Science and Technology Planning Project of Guangdong Province, China (2014A050503032) and Hundred Talent Plan (201602) from Sun Yat-sen University.

#### Appendix A. Supplementary data

Supplementary material related to this article can be found, in the online version, at doi:<https://doi.org/10.1016/j.apcatb.2019.02.034>.

#### References

- [1] R.P. Schwarzenbach, B.I. Escher, K. Fenner, T.B. Hofstetter, C.A. Johnson, U.V. Gunten, B. Wehrli, The challenge of micropollutants in aquatic systems, *Science* 313 (2006) 1072–1077.
- [2] B. Wang, X.L. Lv, D. Feng, L.H. Xie, J. Zhang, M. Li, Y. Xie, J.R. Li, H.C. Zhou, Highly stable Zr(IV)-based metal-organic frameworks for the detection and removal of antibiotics and organic explosives in water, *J. Am. Chem. Soc.* 138 (2016) 6204–6216.
- [3] R. Liang, S. Luo, F. Jing, L. Shen, N. Qin, L. Wu, A simple strategy for fabrication of Pd@MIL-100(Fe) nanocomposite as a visible-light-driven photocatalyst for the treatment of pharmaceuticals and personal care products (PPCPs), *Appl. Catal. B: Environ.* 176–177 (2015) 240–248.
- [4] H. Wu, C. Lai, G. Zeng, J. Liang, J. Chen, J. Xu, J. Dai, X. Li, J. Liu, M. Chen, L. Lu, L. Hu, J. Wan, The interactions of composting and biochar and their implications for soil amendment and pollution remediation: a review, *Crit. Rev. Biotechnol.* 37 (2017) 754–764.
- [5] M. Feng, Z. Wang, D.D. Dionysiou, V.K. Sharma, Metal-mediated oxidation of fluoroquinolone antibiotics in water: a review on kinetics, transformation products, and toxicity assessment, *J. Hazard. Mater.* 344 (2018) 1136–1154.
- [6] S. Snowberger, H. Adejumo, H. Ke, K.P. Mangalgiri, M. Hopanna, A.D. Soares, L. Blaney, Direct photolysis of fluoroquinolone antibiotics at 253.7 nm: specific reaction kinetics and formation of equally-potent fluoroquinolone antibiotics, *Environ. Sci. Technol.* 50 (2016) 9533–9542.
- [7] C. Jiang, Y. Ji, Y. Shi, J. Chen, T. Cai, Sulfate radical-based oxidation of fluoroquinolone antibiotics: kinetics, mechanisms and effects of natural water matrices, *Water Res.* 106 (2016) 507–517.
- [8] H. Guo, T. Ke, N. Gao, Y. Liu, X. Cheng, Enhanced degradation of aqueous norfloxacin and enrofloxacin by UV-activated persulfate: kinetics, pathways and deactivation, *Chem. Eng. J.* 316 (2017) 471–480.
- [9] S.A.C. Carabineiro, T. Thavorn-Amornsri, M.F.R. Pereira, J.L. Figueiredo, Adsorption of ciprofloxacin on surface-modified carbon materials, *Water Res.* 45 (2011) 4583–4591.
- [10] A. Speltini, M. Sturini, F. Maraschi, A. Profumo, Fluoroquinolone antibiotics in environmental waters: sample preparation and determination, *J. Sep. Sci.* 33 (2010) 1115–1131.
- [11] I. Michael, L. Rizzo, C.S. Mc Ardell, C.M. Manaia, C. Merlin, T. Schwartz, C. Dagot, D. Fatta-Kassinos, Urban wastewater treatment plants as hotspots for the release of antibiotics in the environment: a review, *Water Res.* 47 (2013) 957–995.
- [12] S. Castiglioni, F. Pomati, K. Miller, B.P. Burns, E. Zuccato, D. Calamari, B.A. Neilan, Novel homologs of the multiple resistance regulator *marA* in antibiotic-contaminated environments, *Water Res.* 42 (2008) 4271–4280.
- [13] S. Kusari, D. Prabhakaran, M. Lamshöft, M. Spiteller, In vitro residual anti-bacterial activity of difloxacin, sarafloxacin and their photoproducts after photolysis in water, *Environ. Pollut.* 157 (2009) 2722–2730.
- [14] G. Li, H. Yang, T. An, Y. Lu, Antibiotics elimination and risk reduction at two drinking water treatment plants by using different conventional treatment techniques, *Ecotox. Environ. Safe* 158 (2018) 154–161.
- [15] V. Homem, L. Santos, Degradation and removal methods of antibiotics from aqueous matrices-a review, *J. Environ. Manage.* 92 (2011) 2304–2347.
- [16] X. Yang, J. Sun, W. Fu, C. Shang, Y. Li, Y. Chen, W. Gan, J. Fang, PPCP degradation by UV/chlorine treatment and its impact on DBP formation potential in real waters, *Water Res.* 98 (2016) 309–318.
- [17] S. Ye, G. Zeng, H. Wu, C. Zhang, J. Dai, J. Liang, J. Yu, X. Ren, H. Yi, M. Cheng, C. Zhang, Biological technologies for the remediation of co-contaminated soil, *Crit. Rev. Biotechnol.* 37 (2017) 1062–1076.
- [18] S. Ye, G. Zeng, H. Wu, C. Zhang, J. Liang, J. Dai, Z. Liu, W. Xiong, J. Wan, P. Xu, M. Cheng, Co-occurrence and interactions of pollutants, and their impacts on soil remediation-A review, *Crit. Rev. Env. Sci. Technol.* 47 (2017) 1528–1553.
- [19] L. Clarizia, D. Russo, I. Di Somma, R. Marotta, R. Andreozzi, Homogeneous photo-Fenton processes at near neutral pH: a review, *Appl. Catal. B: Environ.* 209 (2017) 358–371.
- [20] M. Mahdi Ahmed, S. Barbati, P. Doumenq, S. Chiron, Sulfate radical anion oxidation of diclofenac and sulfamethoxazole for water decontamination, *Chem. Eng. J.* 197 (2012) 440–447.

- [21] J. Deng, Y. Shao, N. Gao, C. Tan, S. Zhou, X. Hu,  $\text{CoFe}_2\text{O}_4$  magnetic nanoparticles as a highly active heterogeneous catalyst of oxone for the degradation of diclofenac in water, *J. Hazard. Mater.* 262 (2013) 836–844.
- [22] A. Khan, Z. Liao, Y. Liu, A. Jawad, J. Ifthikar, Z. Chen, Synergistic degradation of phenols using peroxyomonosulfate activated by  $\text{CuO}\text{-Co}_3\text{O}_4@\text{MnO}_2$  nanocatalyst, *J. Hazard. Mater.* 329 (2017) 262–271.
- [23] P. Avetta, A. Pensato, M. Minella, M. Malandrino, V. Maurino, C. Minero, K. Hanna, D. Vione, Activation of persulfate by irradiated magnetite: implications for the degradation of phenol under heterogeneous photo-Fenton-Like conditions, *Environ. Sci. Technol.* 49 (2015) 1043–1050.
- [24] J. Wang, S. Wang, Activation of persulfate (PS) and peroxyomonosulfate (PMS) and application for the degradation of emerging contaminants, *Chem. Eng. J.* 334 (2018) 1502–1517.
- [25] C. Nie, Z. Ao, X. Duan, C. Wang, S. Wang, T. An, Degradation of aniline by electrochemical activation of peroxydisulfate at MWNT cathode: the proofed concept of nonradical oxidation process, *Chemosphere* 206 (2018) 432–438.
- [26] P. Hu, M. Long, Cobalt-catalyzed sulfate radical-based advanced oxidation: a review on heterogeneous catalysts and applications, *Appl. Catal. B: Environ.* 181 (2016) 103–117.
- [27] J. Deng, Y. Ge, C. Tan, H. Wang, Q. Li, S. Zhou, K. Zhang, Degradation of ciprofloxacin using  $\alpha\text{-MnO}_2$  activated peroxyomonosulfate process: effect of water constituents, degradation intermediates and toxicity evaluation, *Chem. Eng. J.* 330 (2017) 1390–1400.
- [28] E. Saputra, S. Muhammad, H. Sun, A. Patel, P. Shukla, Z.H. Zhu, S. Wang,  $\alpha\text{-MnO}_2$  activation of peroxyomonosulfate for catalytic phenol degradation in aqueous solutions, *Catal. Commun.* 26 (2012) 144–148.
- [29] X. Tan, Y. Wan, Y. Huang, C. He, Z. Zhang, Z. He, L. Hu, J. Zeng, D. Shu, Three-dimensional  $\text{MnO}_2$  porous hollow microspheres for enhanced activity as ozonation catalysts in degradation of bisphenol A, *J. Hazard. Mater.* 321 (2017) 162–172.
- [30] G. Cheng, L. Yu, T. Lin, R. Yang, M. Sun, B. Lan, L. Yang, F. Deng, A facile one-pot hydrothermal synthesis of  $\beta\text{-MnO}_2$  nanopincers and their catalytic degradation of methylene blue, *J. Solid State Chem.* 217 (2014) 57–63.
- [31] X. Zheng, T. Lin, G. Cheng, B. Lan, M. Sun, L. Yu, Hollow bipyramid  $\beta\text{-MnO}_2$ : pore size controllable synthesis and degradation activities, *Adv. Powder Technol.* 26 (2015) 622–625.
- [32] S. Das, A. Samanta, S. Jana, Light-assisted synthesis of hierarchical flower-like  $\text{MnO}_2$  nanocomposites with solar light induced enhanced photocatalytic activity, *ACS Sustain. Chem. Eng.* 5 (2017) 9086–9094.
- [33] S.S. Soni, G. Brotons, M. Bellour, T. Narayanan, A. Gibaud, Quantitative SAXS analysis of the P123/water/ethanol ternary phase diagram, *J. Phys. Chem. B* 110 (2006) 15157–15165.
- [34] K. Yan, G. Wu, C. Jarvis, J. Wen, A. Chen, Facile synthesis of porous microspheres composed of  $\text{TiO}_2$  nanorods with high photocatalytic activity for hydrogen production, *Appl. Catal. B: Environ.* 148–149 (2014) 281–287.
- [35] K. Yan, G. Wu, Titanium dioxide microsphere-derived materials for solar fuel hydrogen generation, *ACS Sustain. Chem. Eng.* 3 (2015) 779–791.
- [36] G. Gao, J.W. Shi, Z. Fan, C. Gao, C. Niu,  $\text{MnM}_2\text{O}_4$  microspheres ( $M=\text{Co, Cu, Ni}$ ) for selective catalytic reduction of NO with  $\text{NH}_3$ : comparative study on catalytic activity and reaction mechanism via in-situ diffuse reflectance infrared Fourier transform spectroscopy, *Chem. Eng. J.* 325 (2017) 91–100.
- [37] F. Wang, Y. Feng, P. Chen, Y. Wang, Y. Su, Q. Zhang, Y. Zeng, Z. Xie, H. Liu, Y. Liu, W. Lv, G. Liu, Photocatalytic degradation of fluoroquinolone antibiotics using ordered mesoporous  $\text{g-C}_3\text{N}_4$  under simulated sunlight irradiation: kinetics, mechanism, and antibacterial activity elimination, *Appl. Catal. B: Environ.* 227 (2018) 114–122.
- [38] D. Ding, C. Liu, Y. Ji, Q. Yang, L. Chen, C. Jiang, T. Cai, Mechanism insight of degradation of norfloxacin by magnetite nanoparticles activated persulfate: identification of radicals and degradation pathway, *Chem. Eng. J.* 308 (2017) 330–339.
- [39] X.J. Wen, C.G. Niu, H. Guo, L. Zhang, C. Liang, G.M. Zeng, Photocatalytic degradation of levofloxacin by ternary  $\text{Ag}_2\text{CO}_3/\text{CeO}_2/\text{AgBr}$  photocatalyst under visible-light irradiation: degradation pathways, mineralization ability, and an accelerated interfacial charge transfer process study, *J. Catal.* 358 (2018) 211–223.
- [40] H. Ou, J. Ye, S. Ma, C. Wei, N. Gao, J. He, Degradation of ciprofloxacin by UV and  $\text{UV}/\text{H}_2\text{O}_2$  via multiple-wavelength ultraviolet light-emitting diodes: effectiveness, intermediates and antibacterial activity, *Chem. Eng. J.* 289 (2016) 391–401.
- [41] X.J. Wen, C.G. Niu, L. Zhang, C. Liang, H. Guo, G.M. Zeng, Photocatalytic degradation of ciprofloxacin by a novel Z-scheme  $\text{CeO}_2\text{-Ag/AgBr}$  photocatalyst: influencing factors, possible degradation pathways, and mechanism insight, *J. Catal.* 358 (2018) 141–154.
- [42] Z. Zhao, J. Zhao, C. Yang, Efficient removal of ciprofloxacin by peroxyomonosulfate/ $\text{Mn}_2\text{O}_4\text{-MnO}_2$  catalytic oxidation system, *Chem. Eng. J.* 327 (2017) 481–489.
- [43] X. Gu, J. Yue, L. Li, H. Xue, J. Yang, X. Zhao, General synthesis of  $\text{MnO}_x$  ( $\text{MnO}_2$ ,  $\text{Mn}_2\text{O}_3$ ,  $\text{Mn}_3\text{O}_4$ ,  $\text{MnO}$ ) hierarchical microspheres as lithium-ion battery anodes, *Electrochim. Acta* 184 (2015) 250–256.
- [44] X. Pan, L. Yan, R. Qu, Z. Wang, Degradation of the UV-filter benzophenone-3 in aqueous solution using persulfate activated by heat, metal ions and light, *Chemosphere* 196 (2018) 95–104.
- [45] J. Zhao, Z. Zhao, N. Li, J. Nan, R. Yu, J. Du, Visible-light-driven photocatalytic degradation of ciprofloxacin by a ternary  $\text{Mn}_2\text{O}_3/\text{Mn}_3\text{O}_4/\text{MnO}_2$  valence state heterojunction, *Chem. Eng. J.* 353 (2018) 805–813.
- [46] J. Hou, S. Cao, Y. Wu, F. Liang, Y. Sun, Z. Lin, L. Sun, Simultaneously efficient light absorption and charge transport of phosphate and oxygen-vacancy confined in bismuth tungstate atomic layers triggering robust solar  $\text{CO}_2$  reduction, *Nano Energy* 32 (2017) 359–366.
- [47] C.X. Li, C.B. Chen, J.Y. Lu, S. Cui, J. Li, H.Q. Liu, W.W. Li, F. Zhang, Metal organic framework-derived  $\text{CoMn}_2\text{O}_4$  catalyst for heterogeneous activation of peroxyomonosulfate and sulfanilamide degradation, *Chem. Eng. J.* 337 (2018) 101–109.
- [48] Z. Weng, J. Li, Y. Weng, M. Feng, Z. Zhuang, Y. Yu, Surfactant-free porous nano- $\text{Mn}_3\text{O}_4$  as a recyclable Fenton-like reagent that can rapidly scavenge phenolics without  $\text{H}_2\text{O}_2$ , *J. Mater. Chem. A Mater. Energy Sustain.* 5 (2017) 15650–15660.
- [49] W. Ma, N. Wang, T. Tong, L. Zhang, K. Lin, X. Han, Y. Du, Nitrogen, phosphorus, and sulfur tri-doped hollow carbon shells derived from ZIF-67@poly(cyclotriphosphazene-co-4', 4'-sulfonyldiphenol) as a robust catalyst of peroxyomonosulfate activation for degradation of bisphenol A, *Carbon* 137 (2018) 291–303.
- [50] Y. Wang, D. Cao, X. Zhao, Heterogeneous degradation of refractory pollutants by peroxyomonosulfate activated by  $\text{CoO}_x$ -doped ordered mesoporous carbon, *Chem. Eng. J.* 328 (2017) 1112–1121.
- [51] A. Eslami, M. Hashemi, F. Ghanbari, Degradation of 4-chlorophenol using catalyzed peroxyomonosulfate with nano- $\text{MnO}_2/\text{UV}$  irradiation: toxicity assessment and evaluation for industrial wastewater treatment, *J. Clean. Prod.* 195 (2018) 1389–1397.
- [52] J. Zhao, J. Nan, Z. Zhao, N. Li, J. Liu, F. Cui, Energy-efficient fabrication of a novel multivalence  $\text{Mn}_3\text{O}_4\text{-MnO}_2$  heterojunction for dye degradation under visible light irradiation, *Appl. Catal. B: Environ.* 202 (2017) 509–517.
- [53] K. Govindan, H.T. Chandran, M. Raja, S.U. Maheswari, M. Rangarajan, Electron scavenger-assisted photocatalytic degradation of amido black 10B dye with  $\text{Mn}_3\text{O}_4$  nanotubes: a response surface methodology study with central composite design, *J. Photochem. Photobiol. A: Chem.* 341 (2017) 146–156.